Letters

Data-Driven Adaptive Open-Circuit Fault Localization Method With Reduced Sensors for Magnetic-Network Energy Router

Weiheng Zeng and Sayed Abulanwar, *Senior Member, IEEE*

***Abstract*—Fault localization is a critical challenge for magnetic-network energy router (MNER) consisting of numerous switches. This letter proposes a data-driven adaptive open-circuit fault localization method with reduced sensors for MNER. Through the extraction of adaptive data ensembles from interarm voltage sampling channels, numerous time-sliding ensemble anomaly encoders (EAEs) are constructed to isolate the abnormal channels. Next, by means of buffering and decoding the EAE's output, the faulty switch can be effectively localized. The proposed method not only reduces fault feature dimensionality, thereby minimizing the requirement for extra hardware, but also eliminates the reliance on mathematical model and threshold setting. A 2-kW MNER experimental platform is constructed to verify the effectiveness of the proposed method.**

***Index Terms*—Data-driven, fault localization, magnetic network energy router (MNER), open-circuit fault (OCF).**

I. Introduction

MAGNETIC-NETWORK energy router (MNER) has emerged as a focus of interest in the family of isolated multiport dc–dc converters, due to its unique advantages of reliable electrical isolation and highly integrated design [1], [2], [3], [4]. Reliability is crucial for MNER, which consists of numerous power electronic switches. Each switch can trigger a potential open-circuit fault (OCF), generating the overcurrent and transformer saturation, causing secondary damage. Therefore, an efficient OCF localization method is vital for the safe operation of MNER [5].

The methods of OCF localization in isolated multiport dc–dc converters can be broadly classified into two categories: model-based method and data-based methods. The model-based methods rely on the math models to describe the normal and faulty behaviors, by applying Kalman filter and other state observers for fault localization [6], [7]. The model-based methods require constructing precise model of MNER. However, the characteristics of nonlinear and magnetic-coupling within MNER not only complicates the modelling, but also demands computational resources and introduce delays in the localization process. In addition, the model-based methods require manual threshold setting, which depends on trial-and-error adjustments, leading to degrading localization performance under the operation condition variations.

Data-based method is another category, which avoids constructing complex mathematical model in contrast with model-based ones. In [8], the ac-side voltage of transformer is applied in fault detection, but it fails to localize faults in specific switches. In [9], auxiliary windings and current sensors are introduced to detect primary-side voltage, which increases hardware cost. In [10], [11], and [12], the arm voltage and inductor current are applied as diagnosis criteria, but it requires individual voltage sensors and current sensors installed on every arm, imposing hardware overhead. Several artificial intelligence methods, such as finite state machines [13] and neural networks [14], have been adopted for fault localization for dual-active bridge converter. However, these methods fail to effectively address multiswitch faults, and their complex computational requirements affect the efficiency of fault localization. Moreover, the existing data-based methods still require manual threshold setting, hindering their feasibility.

To address the above issues of complicated modeling, threshold setting, and hardware overhead associated with existing methods, this letter proposes a data-driven adaptive fault localization method for MNER. First, the data windows of interarm voltages (IVs) are employed as input channels for ensemble anomaly encoders (EAEs). Subsequently, the data features such as the baseline mean and standard deviation of each channel are adaptively established. After that, these features are fed into the EAEs and determine the EAE's outputs (EAEOs), by calculating the mean depth (MD) of each channel. Finally, the fault switch is localized through buffering and decoding the EAEOs.

The primary contributions of the proposed method include the following.

1) It decreases hardware costs through the reduction of voltage sensors and eliminating auxiliary windings compared

Received 31 May 2025; revised 16 July 2025; accepted 8 August 2025. Date of publication 13 August 2025; date of current version 22 October 2025. This work was supported in part by the National Key Research and Development Program of China under Grant 2022YFE0196300 and in part by the Science, Technology & Innovation Funding Authority (STDF) under Grant 46505. *(Corresponding author: Weiheng Zeng.)*

Weiheng Zeng is with the School of Electrical Engineering, Southeast University, Nanjing 210096, China (e-mail: 220243062@seu.edu.cn).

Sayed Abulanwar is with the Department of Electrical Engineering, Faculty of Engineering, Mansoura University, Mansoura 35516, Egypt, and also with the Department of Electronic and Electrical Engineering, University of Strathclyde, Manama 346, Kingdom of Bahrain (e-mail: abulanwar@mans.edu.eg).

Color versions of one or more figures in this article are available at https://doi.org/10.1109/TPEL.2025.3598349.

Digital Object Identifier 10.1109/TPEL.2025.3598349

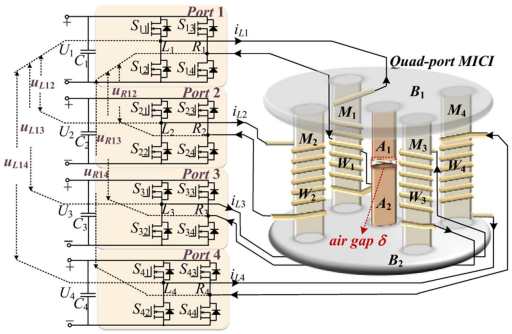

Fig. 1. Topology structure of quad-port MNER.

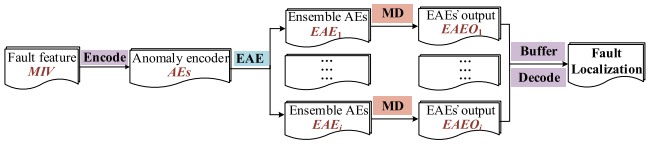

Fig. 2. Proposed data-driven adaptive fault localization method for MNER.

with [6], [7], [8], [9], [10] and [12], due to the innovative utilization of the relationship among IVs.

2) It enhances the speed and accuracy of fault localization, by directly employing lightweight anomaly encoder (AE) and leveraging the sparsity-based fault identification, instead of setting thresholds and conducting complicated models in contrast with [6], [7], [8], [9], [10], [11] and [12].
3) It innovatively enables concurrent multiswitch fault localization through a scalable composite decoder in contrast with [13] and [14].

II. Quad-Port Magnetic-Network Energy Router

Fig. 1 shows the topology structure of a quad-port MNER where four full-bridges are linked by the magnetic integrated coupled inductor (MICI), which reduces the size and elevates power density of MNER. The MICI is composed of four windings $W_1 \sim W_4$ wound on corresponding magnetic columns $M_1 \sim M_4$. The columns $M_1 \sim M_4$ feature an annular region $A_1 \sim A_2$ with an interposed air gap δ, and position between two cylindrical disks $B_1 \sim B_2$. The windings $W_1 \sim W_4$ are respectively connected to the ac side of ports 1–4, while $i_{L1} \sim i_{L4}$ denote the corresponding currents flowing through the windings. Each bridge in MNER contains four switches, and capacitors $C_1 \sim C_4$ are parallelly connected to dc voltages $U_1 \sim U_4$. With port 1 serving as the reference, $u_{L12} \sim u_{L14}$, $u_{R12} \sim u_{R14}$ respectively denote the IVs of ports 2–4 in relation to u_{L1}, u_{R1}.

III. Proposed Data-Driven Fault Localization Method

Normally, complicated modeling and threshold setting are required for fault localization, degrading its speed and accuracy. To address the issue, the data-driven adaptive fault localization method is proposed for MNER, as shown in Fig. 2. First, the fault feature of IVs is extracted and averaged into mean interarm voltages (MIVs) using sliding-time window (STW). Subsequently, the AEs are constructed by establishing adaptive

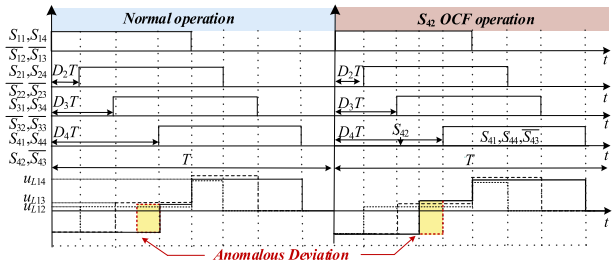

Fig. 3. Waveforms of drive signals, mid-point voltages and IVs.

baseline mean and standard deviation of MIVs. Furthermore, the EAE for MNER is constructed based on neighboring AEs. Afterwards, determined by the MD within AEs, the EAEO is being continuously buffered and decoded to achieve final localization.

A. MIV-Based Fault Feature Selection

Fig. 3 shows the waveforms of drive signals and IVs under single-phase shift (SPS) modulated MNER, during both normal operation and OCF operation. T stands for the switching period. Under normal operation, each u_{L1i} (i = 2,3,4) in the SPS-modulated MNER successively lags behind by phase-shift angles $D2 \sim D4$. However, once OCF occurs to S_{42}, its corresponding drive signal is simultaneously disabled. As a result, the u_{L14} associated with S_{42} is forced into an unbalanced state, generating a sustained anomalous deviation. Notably, the deviation exhibits complementary half-cycle identity to the right-arm waveforms u_{R1i} (i = 2,3,4).

Within each full-bridge of MNER, when i_{Li} (i = 1, 2, 3, 4) flows through the upper bridge arm, the corresponding arm voltage equals to the dc voltage of its associated port, and becomes zero when i_{Li} passes through the lower arm. Under normal operating conditions, the switches in both upper and lower bridge arms maintain symmetrical conduction time of half a cycle each. As shown in Fig. 3, each MIV under normal operation can be obtained as

$$\begin{aligned} U_{L1i\_N} = U_{R1i\_N} &= \frac{\int_0^{D_iT} u_{L1i}(t)}{T} + \frac{\int_{D_iT}^{T/2-D_iT} u_{L1i}(t)}{T} \\ &+ \frac{\int_{T/2-D_iT}^{T/2} u_{L1i}(t)}{T} \\ &= -D_iU_1 + \left(\frac{1}{2} - D_i\right)(U_i - U_1) + D_iU_i = \frac{U_i - U_1}{2} \end{aligned} \tag{1}$$

where U_{L1i_N} and U_{R1i_N} stands for the MIV of left and right arm respectively under normal operation.

Conversely, after an OCF, MIV exhibits abnormal deviation, as given in Table I, due to the nonidentical conduction time between upper and lower arms. Because the deviation emerges only under OCF and not presents during normal operation, the MIVs could be selected as fault feature to be analyzed in EAE to achieve fault localization.

TABLE I
MEAN VALUE OF INTERARM VOLTAGE UNDER FAULTS

Fault position	Faulty switch	Fault feature	Range
Upper arm	S_{i1}	U_{L1i}	$<U_{L1i\_N}$
	S_{i3}	U_{R1i}	$<U_{R1i\_N}$
Lower arm	S_{i2}	U_{L1i}	$>U_{L1i\_N}$
	S_{i4}	U_{R1i}	$>U_{R1i\_N}$

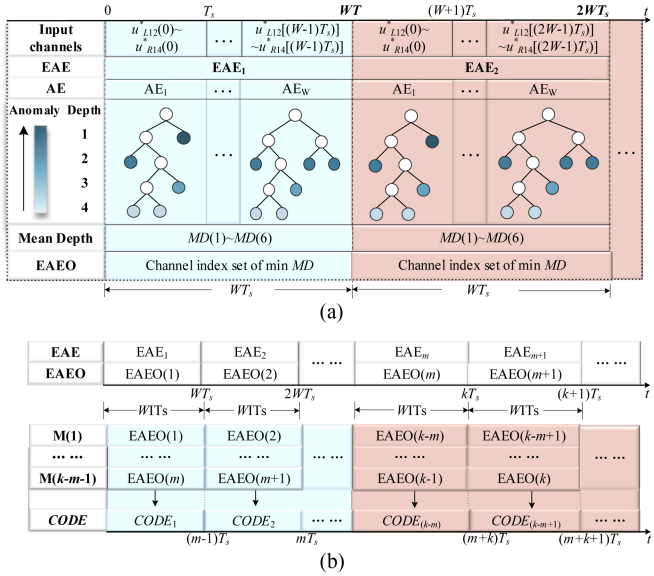

Fig. 4. EAE for MNER. (a) AEs and EAEs. (b) Buffer ***M*** and *CODE*.

B. AE for MNER

As shown in Fig. 4(a), an AE is a nonlinear data structure, containing a number of levels. Each level is composed of the nodes, where each node is separated into two subnodes in the next level. Finally, each AE has six terminal nodes located at the layer terminals, which store the data of corresponding sampling channels and cannot be further divided.

Furthermore, the numerous AEs are established based on the input vector composed of six sampling channels representing the normalized mean interarm voltages (NMIVs): $U^*_{L12}\sim U^*_{L14}$, $U^*_{R12}\sim U^*_{R14}$, defined as

$$\begin{cases} U^*_{L1i} = \dfrac{2U_{L1i}-(U_j-U_1)}{|U_j-U_1|} = \dfrac{2U_{L1i}}{|U_j-U_1|} \pm 1 \\ U^*_{R1i} = \dfrac{2U_{R1i}-(U_j-U_1)}{|U_j-U_1|} = \dfrac{2U_{R1i}}{|U_j-U_1|} \pm 1 \end{cases}. \tag{2}$$

To compute NMIVs, a STW of an fixed length W is employed, which continuously advances and segments the IVs, and converts them into short-term means MIVs. Afterward, MIVs are normalized into NMIVs to achieve dimensional unification among channels.

C. EAE for MNER

An EAE is composed of W neighboring AEs, including $\mathrm{AE}_1\sim \mathrm{AE}_\mathrm{W}$. Fig. 4(a) shows the EAEs for the quad-port MNER. In each EAE, channel$_i$ ($1\le i\le 6$) in the jth AE corresponds with a depth $D(i, j)$, indicating its level position in the jth AE.

Fig. 4(a) also shows the anomalous degree for nodes in EAE with the different colors. Along with the darkening of color, the nodes would have a higher probability to store an anomalous channel, which exhibits smaller level in the EAE in contrast with normal channels.

TABLE II
EAE FOR MNER UNDER FAULT

Switch state	Channel depth	Channel *MD*
Normal	↑	↑
OCF	↓	↓

D. EAE's Output for MNER

The EAEO is defined as the set of index and deviation type of the channels corresponding to the nodes exhibiting smaller MD, as the abnormal nodes in each EAE exhibit a high probability to contain the smaller MD. In each EAE, the MD(λ) of channel$_\lambda$ in a window length W is calculated as

$$\mathrm{MD}(\lambda) = \frac{1}{W}\sum_{j=1}^{W} D(\lambda, j). \tag{3}$$

Following the EAE establishment for MNER, in order to classify the fault candidates in each EAE, the adaptive reference statistics: mean value μ and standard deviation σ for channel$_\lambda$ at the kth sampling periods [15], are computed as

$$\begin{cases} \mu_\lambda(k) = \frac{1}{W}\sum_{a=k-W+1}^{a=k} I_i(a) \\ \sigma_\lambda(k) = \min\left\{\sqrt{\frac{1}{W}\sum_{a=k-W+1}^{a=k}\left(I_i(a)-\mu_i\right)^2}, 0.02\,\mu_i\right\} \end{cases}. \tag{4}$$

The set of fault candidate channels is identified using channel-wise confidence scores $C_\lambda(k)$ [15], determined as

$$\begin{cases} C_\lambda(k) = \frac{|I_\lambda(k)-\mu_\lambda|}{\sigma_i} \\ \Lambda(k) = \left\{\lambda \middle| C_\lambda(k) > \frac{2}{W}\sum_{j=\lambda-W+1}^{\lambda}\left[\frac{1}{6}\sum_{j=1}^{6} C_j(\lambda)\right]\right\} \end{cases} \tag{5}$$

where $\Lambda(k)$ is the set of fault candidates at kth sampling periods.

Channels identified by (4) and (5) as fault candidates exhibit smaller values of *MD* in the EAE, in contrast with those under normal operation, as given in Table II.

Moreover, according to Table I, the deviation direction could be classified into two types as

$$\mathrm{dir}_\lambda = \begin{cases} 1\ C_i(k) < 0, & \text{upper switch fault} \\ 2\ C_i(k) > 0, & \text{lower switch fault} \end{cases} \tag{6}$$

where dir$_\lambda$ links the deviation direction type with switch position.

Consequently, a λth channel fault induces the MD(λ) exhibiting a high probability to be smallest. Finally, the set of indexes λ and deviation types dir$_\lambda$ corresponding to the fault candidate channels in EAE constitutes the EAEO, expressed as

$$\mathrm{EAEO}(k) = \{(\lambda, \mathrm{dir}_\lambda) | \lambda \in \Lambda(k)\}. \tag{7}$$

E. Fault Localization

As shown in Fig. 4(b), each EAE sequentially generates independent EAEO in conjunction with the STW process. In order to monitor fault occurrences and carry fault information

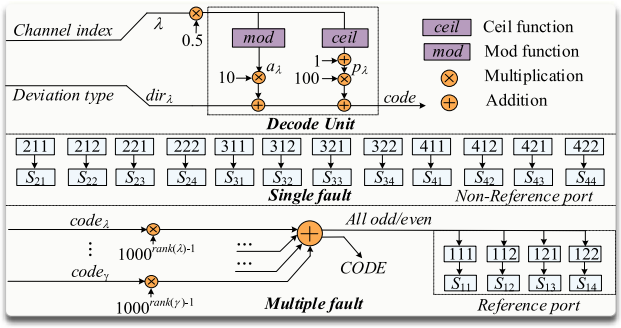

Fig. 5. Composite decoder for fault localization.

in the MNER, a buffer $\boldsymbol{M}$ is created to store m successive EAEOs, which is expressed as

$$\begin{cases} \boldsymbol{M} = \{M(1), M(2), \cdots, M(m-1), M(m)\} \\ M(1) = \text{EAEO}(k-m+1), \cdots, M(m) = \text{EAEO}(k) \end{cases} \tag{8}$$

where $M(1)$, …, $M(m)$ represent m successive elements.

The buffer $\boldsymbol{M}$ is updated every *WTs*, with the oldest EAEO is removed and the newest EAEO is inserted. Upon inspection, if the m neighboring values in the buffer are consistently identical $\boldsymbol{M}(1) = \boldsymbol{M}(2) = \ldots = \boldsymbol{M}(m) = \{\lambda, \text{dir}_\lambda\}$, these abnormal channels with corresponding deviation types are detected.

Based on the buffering result, the composite decoder for fault localization is employed to generate the integer *CODE*, which maps the channel anomaly to switch physical location, as shown in Fig. 5.

1) *Fault Localization of Nonreference Port:* As shown in Fig. 5, after buffering the EAEOs and obtaining λ and dir, function ceil and mod are employed to obtain the variables p_λ and a_λ. Specifically, function ceil and mod, respectively, generate the smallest integer greater than or equal to λ/2, and the residual of λ/2, expressed as

$$p_\lambda = \text{ceil}\left(\frac{\lambda}{2}\right) + 1, a_\lambda = \text{mod}\left(\frac{\lambda}{2}\right) \tag{9}$$

where the symbol p represents the port number ($p = 1, 2, 3, 4$). Symbol a indicates the arm location ($a = 1, 2$), with 1 referring to the left arm and 2 referring to the right arm.

Once the deviation type, port location, and arm location are determined, *code* is generated by incorporating the decimal-weighting coefficients. Subsequently, *CODE* is generated by aggregating these potential *code*s, which are expressed as

$$\begin{cases} \text{code} = 100p_\lambda + 10a_\lambda + \text{dir}_\lambda \\ \text{CODE} = \sum_{\lambda \in \Lambda} \text{code}_\lambda \times 1000^{r(\lambda)-1} \end{cases} \tag{10}$$

where $r(\lambda)$ is the rank of λ within channels by ascending order.

Following *CODE* determination, the physical switch location is uniquely mapped, and a fault flag is triggered to localize the faulty switch.

2) *Fault Localization of Reference Port:* The faulty switch in reference port is localized through group anomaly detection, when all the odd-indexed $U^*_{L12} \sim U^*_{L14}$ or even-indexed $U^*_{R12} \sim U^*_{R14}$ channels are detected as anomalies, as given in Table III. In this case, the corresponding *CODE* is directly

TABLE III
FAULT LOCALIZATION IN REFERENCE PORT

Abnormal group	Deviate direction	Faulty switch	*CODE*
$U^*_{L12} \sim U^*_{L14}$/ $U^*_{R12} \sim U^*_{R14}$	↓	S_{11}/S_{13}	111/121
	↑	S_{12}/S_{14}	112/122

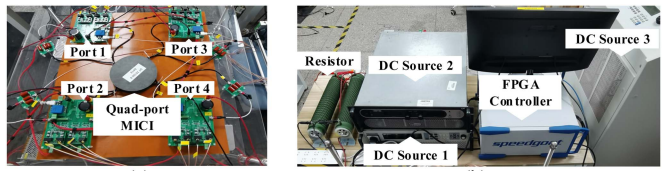

(a) (b)

Fig. 6. Experimental prototype of the quad-port MNER. (a) Quad-port MNER. (b) FPGA controller, power supply, and resistive load.

TABLE IV
EXPERIMENTAL SYSTEM PARAMETERS

Parameters	Details	Parameters	Details
Voltage:U_1,U_2,U_4 (V)	80,60,75	Winding turns: W_1~W_4	3,3,3,3
Switching period: T (μs)	10	Capacitance: C_1~C_4 (μF)	820
Resistance: R_{LD} (Ω)	60	Magnetic material	Ferrite
Buffer length: m	4 Points	Window length: W	10 Points

IV. EXPERIMENTAL VERIFICATION

To verify the proposed method, a quad-port MNER prototype was built, as shown in Fig. 6(a) and (b). In the prototype, port 1, 2, and 4 are connected to dc power supplies U_1, U_2, and U_4 respectively, while port 3 is connected to a resistive load R_{LD}, and sixteen identical SiC MOSFETs are employed.

The prototype parameters of the quad-port MNER are determined in Table IV. Meanwhile, the proposed fault localization method is implemented in the Speedgoat FPGA controller. In order to simulate switch OCF, the drive signal of corresponding MOSFET is set to zero.

A. Case 1: Single-Switch OCF

In this case, OCF occurs to S_{23} in the nonreference port at 50.00 ms. As shown in Fig. 7(a) and (b), initially, IVs exhibit symmetry and NMIVs stabilize near 0, with *CODE* equal to 0. After the S_{23} OCF, u_{R12} waveform distorts, causing U^*_{R12} to deviate negatively. At 50.01 ms, *CODE* is triggered to 221, and faulty switch S_{23} is localized within one switching period.

In this case, OCF occurs to S_{12} in the reference port at 50.00 ms. As shown in Fig. 8(a) and (b), initially, IVs exhibit symmetry and NMIVs stabilize near 0, with *CODE* equal to 0. After fault, all even-indexed NMIVs $U^*_{L12} \sim U^*_{L14}$ deviate positively. Finally, at 50.01 ms, group anomaly detection triggers *CODE* to 112, localizing faulty switch S_{12} within one switching period.

B. Case 2: Single-Switch OCF Under Input-Voltage Change

In this case, under the scenario of S_{23} OCF, the U_2 step-change from 60 to 75 V occurs at 80.00 ms. As shown in Fig. 9(a) and (b), prior to this voltage disturbance, all NMIVs except the abnormal U^*_{R12} stabilize near 0, while U^*_{R12} stabilizes

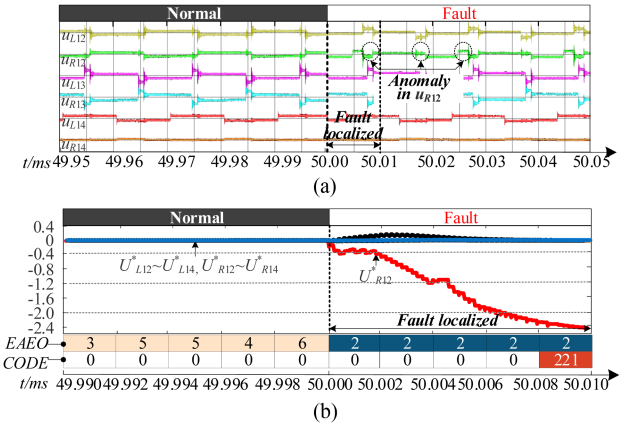

Fig. 7. Experimental waveforms under S_{23} OCF. (a) IVs including u_{L12}~u_{L14} (250 V/div), u_{R12}~u_{R14} (250 V/div), with a time base of 5 μs/div. (b) NMIVs (including U^*_{L12}~U^*_{L14}, U^*_{R12}~U^*_{R14}), EAEO, and *CODE*.

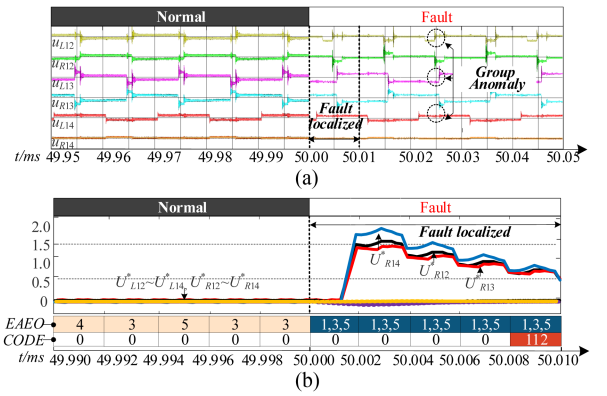

Fig. 8. Experimental waveforms under S_{12} OCF. (a) IVs including u_{L12}~u_{L14} (250 V/div), u_{R12}~u_{R14} (250 V/div), with a time base of 5 μs/div. (b) NMIVs including U^*_{L12}~U^*_{L14}, U^*_{R12}~U^*_{R14}, EAEO, and *CODE*.

the waveform of u_{L12} and u_{L14}, which drives U^*_{L12} and U^*_{L14} to fluctuate gradually. Critically, EAEOs buffering successfully isolates these anomalies in U^*_{L12} and U^*_{L14} induced by voltage disturbance, and the *CODE* stabilizes at 221, ensuring reliable fault localization across input-voltage change.

C. Case 3: Single-Switch OCF Under Load Change

In this case, under the scenario of S_{31} OCF, the step-change of R_{LD} from 60 to 80 Ω occurs at 80.00 ms. As shown in Fig. 10(a) and (b), prior to this load disturbance, all NMIVs except the abnormal U^*_{L13} stabilize near 0, while U^*_{L13} stabilizes near -1, with *CODE* at 311. At 80.00 ms, load disturbance triggers waveform distortion of u_{R13}, which drives U^*_{R13} to fluctuate. Critically, EAEOs buffering successfully isolates this anomaly in U^*_{R13} induced by load disturbance, and the *CODE* stabilizes at 311, ensuring reliable localization across load change.

D. Case 4: Multiswitch OCF

In this case, concurrent multiswitch faults occur to S_{21} and S_{32} at 50.00 ms. As shown in Fig. 11(a) and (b), initially, IVs exhibit symmetry and NMIVs stabilize near 0, with *CODE* equal to 0.

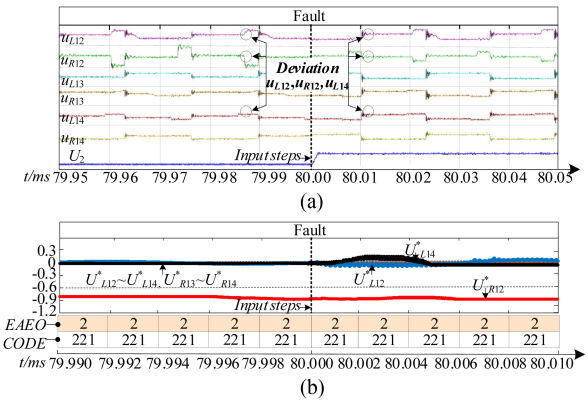

Fig. 9. Experimental waveforms under S_{23} OCF and input-voltage-change. (a) IVs including u_{L12}~u_{L14} (250 V/div) and u_{R12}~u_{R14} (250 V/div), and DC voltage U_2 (100 V/div), with a time base of 5 μs/div. (b) NMIVs (including U^*_{L12}~U^*_{L14}, U^*_{R12}~U^*_{R14}), EAEO, and *CODE*.

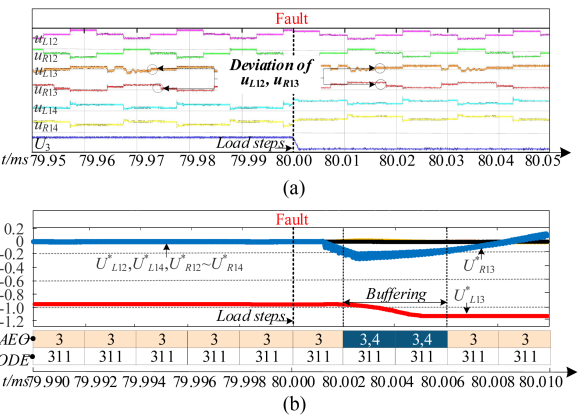

Fig. 10. Experimental waveforms under S_{31} OCF and load-change. (a) IVs including u_{L12}~u_{L14} (250 V/div) and u_{R12}~u_{R14} (250 V/div), and DC voltage U_3 (100 V/div) with a time base of 5 μs/div. (b) NMIVs (including U^*_{L12}~U^*_{L14}, U^*_{R12}~U^*_{R14}), EAEO, and *CODE*.

Following the concurrent fault occurrence in S_{21} and S_{32}, U^*_{L12} and U^*_{R13} exhibit positive and negative deviation, respectively. Finally, at 50.02 ms, group anomaly detection triggers *CODE* to 211312, achieving multifault localization of faulty switch S_{21} and S_{32} within two switching period.

E. Comparison of Fault Localization Methods

Table V gives the comparison of the proposed method and typical existing methods [6], [9], [10], [12], [14] applied in quad-port MNER, evaluating seven key metrics: math models; threshold setting; extra hardware; localization time; multifaults localization; data volume; and computational burden.

In contrast with the existing methods, this proposed method achieves following significant benefits.

1) Extra hardware cost is reduced based on the innovative feature extraction of IVs.
2) Accurate localization is achieved within one switching period, by means of leveraging the sparsity-based fault candidate identification and direct statistical analysis, instead of mathematical modeling or threshold setting.

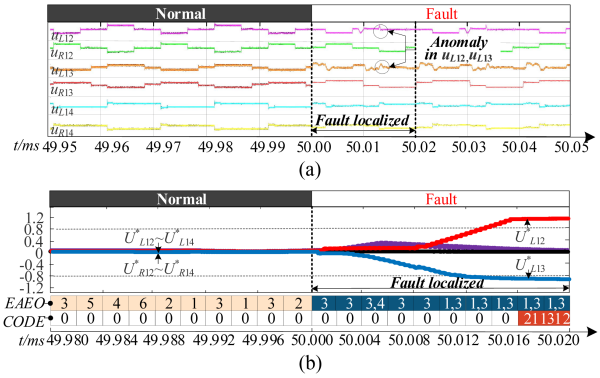

Fig. 11. Experimental waveforms under S_{21} and S_{32} OCF. (a) IVs including u_{L12}~u_{L14} (250 V/div) and u_{R12}~u_{R14} (250 V/div), with a time base of 5 μs/div. (b) NMIVs (including U^*_{L12}~U^*_{L14}, U^*_{R12}~U^*_{R14}), EAEO, and *CODE*.

TABLE V
COMPARISON OF FAULT LOCALIZATION METHODS

Method	Zhuo et al. [6]	Shi et al. [9]	Zheng et al. [10]	Yang et al. [12]	Xing et al. [14]	**Proposed method**
Math Models	Yes	Yes	No	No	No	**No**
Threshold Setting	Yes	Yes	Yes	Yes	Yes	**No**
Extra Hardware	8 sensors	8 sensors	4 sensors & 3 windings	8 sensors	8 sensors	**6 sensors**
Multi-Faults Localization	No	No	No	No	No	**Yes**
Data Volume	Large	Large	Medium	Medium	Large	**Low**
Computational Burden	Medium	High	Medium	High	High	**Medium**
Localization Time	3T	3T	2T	2T	2T	***T***

3) Computational burden and data volume are alleviated, through the employment of the lightweight-anomaly-encoder-based inference.
4) Concurrent multiswitch faults are effectively addressed, through scalable composite decoder.

V. CONCLUSION

In this letter, a rapid and reliable data-driven adaptive switch OCF localization method is proposed for MNER. Numerous EAEs and decoders are constructed using adaptive datasets containing samples of IVs to localize faulty switch within MNER. The proposed method not only reduces hardware cost by minimizing sensor requirements, but also eliminates the mathematical model and manual threshold setting. The experimental results verify the feasibility and effectiveness of the proposed method.

REFERENCES

[1] Y. Chen, P. Wang, Y. Elasser, and M. Chen, "Multicell reconfigurable multi-input multi-output energy router architecture," *IEEE Trans. Power Electron.*, vol. 35, no. 12, pp. 13210–13224, Dec. 2020.
[2] D. Lin, F. Deng, W. Hua, M. Cheng, Z. Chen, and Z. Wang, "High-performance photon-driven PMDC motor system," *Nature Commun.*, vol. 15, no. 1, pp. 1–15, 2024.
[3] Z. Yin et al., "Voltage difference-based model-free predictive control for dual-active-bridge converters," *IEEE Trans. Ind. Electron.*, vol. 35, no. 2, pp. 1957–1966, Feb. 2020, doi: 10.1109/TIE.2025.3589382.
[4] Y. Lv, F. Deng, Z. Shen, S. S. Kaddah, Q. Yu, and S. Abulanwar, "Quad-port magnetic integrated coupled inductor based magnetic network energy routers with high power density," *IEEE Trans. Power Electron.*, vol. 40, no. 8, pp. 11655–11672, Aug. 2025.
[5] S. S. Khan and H. Wen, "A comprehensive review of fault diagnosis and tolerant control in DC-DC converters for DC microgrids," *IEEE Access*, vol. 9, pp. 80100–80127, 2021.
[6] S. Zhuo, Y. Ma, R. Zhang, Y. Huangfu, and F. Gao, "Sliding mode observer-based robust switch fault diagnosis of bidirectional interleaved converters for energy storage system," *IEEE Trans. Power Electron.*, vol. 40, no. 7, pp. 9853–9863, Jul. 2025.
[7] M. Deckers, L. V. Cappellen, J. Moschner, M. Daenen, and J. Driesen, "Real-time MOSFET condition monitoring for variable mission profiles with a dual extended kalman filter," *IEEE Trans. Power Electron.*, vol. 40, no. 1, pp. 2219–2234, Jan. 2025.
[8] D. Xie and X. Ge, "Open-circuit fault diagnosis of dual active bridge DC-DC converter based on residual analysis," in *Proc. IEEE Int. Power Electron. Appl. Conf. Expo.*, 2018, pp. 1–6.
[9] H. Shi, H. Wen, G. Chen, Q. Bu, G. Chu, and Y. Zhu, "Multiple-fault-tolerant dual active bridge converter for DC distribution system," *IEEE Trans. Power Electron.*, vol. 37, no. 2, pp. 1748–1760, Feb. 2022.
[10] M. Zheng, H. Wen, H. Shi, Y. Hu, Y. Yang, and Y. Wang, "Open-circuit fault diagnosis of dual active bridge DC-DC converter with extended-phase-shift control," *IEEE Access*, vol. 7, pp. 23752–23765, 2019.
[11] H. Wen, J. Li, H. Shi, Y. Hu, and Y. Yang, "Fault diagnosis and tolerant control of dual-active-bridge converter with triple-phase shift control for bidirectional EV charging systems," *IEEE Trans. Transport. Electrific.*, vol. 7, no. 1, pp. 287–303, Jan. 2021.
[12] W. Yang, J. Ma, M. Zhu, and C. Hu, "Open-circuit fault diagnosis and tolerant method of multiport Triple active-bridge DC-DC converter," *IEEE Trans. Ind. Appl.*, vol. 59, no. 5, pp. 5473–5487, May 2023.
[13] S. S. Khan and H. Wen, "A fast and low-cost open-circuit fault detection and isolation technique for three-phase dual-active-bridge converters based on finite State machines," *IEEE Trans. Power Electron.*, vol. 39, no. 2, pp. 2751–2766, Feb. 2024.
[14] Z. Xing, J. Chen, Y. Zhao, Y. Fu, Y. He, and W. Zhang, "An online open-switch fault diagnosis method for the DAB converter based on multimodal fusion neural controlled differential equations," *IEEE Trans. Instrum. Meas.*, vol. 72, 2023, Art. no. 3503211.
[15] C. Li, L. Guo, H. Gao, and Y. Li, "Similarity-measured isolation forest: Anomaly detection method for machine monitoring data," *IEEE Trans. Instrum. Meas.*, vol. 70, 2021, Art. no. 3512512.